Journal of Materials Chemistry A

PAPER

Cite this: J. Mater. Chem. A, 2015, 3, 12530

Controllable synthesis of 3D binary nickel–cobalt hydroxide/graphene/nickel foam as a binder-free electrode for high-performance supercapacitors†

Yang Bai, Weiqi Wang, Ranran Wang, Jing Sun* and Lian Gao

Received 11th March 2015
Accepted 6th May 2015

DOI: 10.1039/c5ta01804h

www.rsc.org/MaterialsA

Binder-free electrodes based on 3D porous nickel–cobalt binary hydroxides (NCH)/graphene (G) composites on nickel foam (NF) for supercapacitors are fabricated *via* a chemical vapor deposition (CVD) process combined with an electrochemical deposition (ED) method. High quality graphene grown on NF makes the surface more suitable for deposition of 3D porous NCH and simultaneously enhances the electrode conductivity. The 3D structure can improve the electron transport ability and increase the contact of the active sites with electrolyte. The morphology and electrochemical performance of NCH/G/NF electrodes can be readily manipulated by adjusting the deposition current density and the Ni–Co ratio of the deposition solution. High capacitance with enhanced stability and rate capability is achieved and is attributed to the synergetic effect of the above factors. Specifically, at the deposition current density of 0.625 mA cm^{-2} and Ni–Co ratio of 1 : 1, the NCH11/G/NF electrode exhibits a maximum specific capacitance of 1410 F g^{-1} at 2 A g^{-1}. When the current density increases to 4 A g^{-1}, the capacitance is still 1328 F g^{-1} with a high capacitance retention of 94.2%. After 2500 cycles, the capacitance retention is 92.1%, which is higher than that of a common slurry-coated electrode. To research its practical applications, an asymmetric supercapacitor was fabricated with a NCH11/G/NF electrode as the positive electrode and activated carbon as the negative electrode. The asymmetric device exhibits a prominent energy density of 33.75 W h kg^{-1} at a power density of 750 W kg^{-1}. The binder-free electrode with superior performance has been proven to be very promising for energy storage.

1. Introduction

In recent years, renewable and clean energies such as solar, wind, and wave energy have been quickly exploited to resolve the increasingly serious energy crisis and environmental issues. At the same time, efficient energy storage devices with high energy and power densities are urgently demanded. Supercapacitors (SCs), also known as electrochemical capacitors, have attracted considerable attention due to their ultra-high power density, long cycling stability, wide operative temperature range, and improved safety.[1,2] However, the energy densities of SCs are much lower than those of batteries, which restrict their wide application and need to be improved. The performance of SCs is primarily determined by the properties of the electrode materials.[3] In order to enhance the energy densities of SCs, electrode materials with high capacitance are required according to the formula of energy density (E) $E = CU^2/2$. Thus far, there are mainly three types of electrode materials for SCs: carbon materials,[4] transition metal oxides/hydroxides,[5–8] and conducting polymer materials.[9] Among them, carbon materials have a large specific surface area, excellent electrical conductivity, and high power densities, while they exhibit low energy densities limited by their adsorption capacity.[10–12] Transition metal oxides/hydroxides possess unique redox properties and high theoretical specific capacitance values. Unfortunately, the key weakness of transition metal oxides/hydroxides is their poor electrical conductivities,[13] leading to low power densities. Consequently, the major challenge for SCs is to improve their energy densities and simultaneously retain their high power densities.

Among various transition metal oxides/hydroxides investigated for SCs, nickel oxides/hydroxides and cobalt oxides/hydroxides with high theoretical capacitance and specific shapes and structures have been extensively researched. The fabrication of binary Ni–Co hydroxides/oxides with a hierarchical architecture is both feasible and promising due to the nearly identical physical and chemical properties and the miscible ions in aqueous solution of nickel and cobalt.[14] In addition, the binary system not only inherits the merits of the individual components, but also yields much higher electrochemical performance. The atomic substitution will increase

The State Key Lab of High Performance Ceramics and Superfine Microstructure, Shanghai Institute of Ceramics, Chinese Academy of Sciences, 1295 Dingxi Road, Shanghai 200050, P.R. China. E-mail: jingsun@mail.sic.ac.cn; liagao@mail.sic.ac.cn; Fax: +86-21-52413122; Tel: +86-21-52414301

† Electronic supplementary information (ESI) available: See DOI: 10.1039/c5ta01804h

electrical conductivity and effectively enhance the active site density and roughness of the final binary product.[15,16] Liu *et al.* synthesized a porous $NiCo_2O_4$ heterostructure array with a high capacitance of 1089 F g^{-1}.[17] Hu *et al.* reported a sol–gel synthesis route of nickel–cobalt oxides, showing a high specific capacitance of 1539 F g^{-1} at 1 A g^{-1}.[13] However, the cycling stability was poor, and the electrode encountered great capacity loss. This phenomenon was probably due to the weak electron transport ability, which was caused by the compact structure and the existence of binder. Recently, many efforts[18–20] have been concentrated on the composites of carbon materials and transition metal oxides/hydroxides to cover the shortage of transition metal oxide/hydroxide materials.

Graphene (G) is a carbon material with a two-dimensional structure, large surface, and integrated conductive network that is suitable for loading other materials.[21] Thus far, reduced graphene oxide (RGO) is commonly used as the matrix for electrode materials due to its high production. With the help of RGO, the capacitance of electrode materials is enhanced.[22,23] However, RGO-based composites show insufficient cycling stability due to the negative effects of the residual oxygen-containing functional groups in RGO. The properties of RGO mainly depend on the synthesis process of RGO, which also affects the stability. Furthermore, an even greater challenge is the conflict between the mass loading of active materials per volume and its utilization efficiency. RGO-based electrodes are commonly binder-enriched by a slurry-coating method. The binder transforms a large portion of active material surface into "dead surface" and decreases the electrical conductivity of electrode materials.[24] Thus, there is a demand for high quality graphene and binder-free electrodes, with the goal of obtaining higher performance of electrodes for SCs.

In this study, high quality graphene (G) grown on nickel foam (NF) *via* chemical vapor deposition (CVD) acted as a matrix. Nickel–cobalt binary hydroxides (NCH) were grown directly on the matrix through an electrochemical deposition (ED) process (Fig. 1). The product could be used as an electrode directly without the addition of binders or any extra treatment.

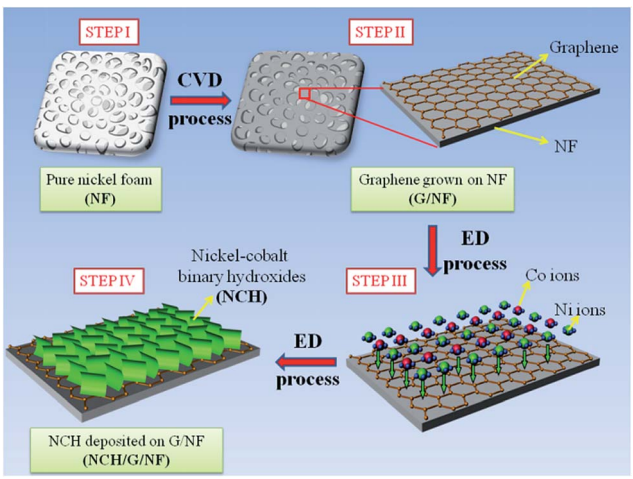

Fig. 1 Schematic illustration of NCH/G/NF preparation.

In the electrode, the high quality graphene with high conductivity provided a network for electron transport. The graphene altered the surface of the matrix so that it was more suitable for growing NCH. As a result, a hierarchical porous 3D NCH structure was obtained, which is beneficial for electrolyte ion transport. The electrodes showed high capacitance with good stability and cyclicity due to the dual advantages of high conductivity and unique structure. The deposition current density had an effect on morphology, and the Ni–Co ratio affected the capacitance and stability.[13,25] After optimal synthesis conditions, the maximum specific capacitance of the NCH/G/NF electrode was as high as 1410 F g^{-1} at 2 A g^{-1}. Moreover, an asymmetric supercapacitor was fabricated to demonstrate the outstanding capacitive behavior of the NCH/G/NF electrode. The asymmetric device exhibited a prominent energy density of 33.75 W h kg^{-1} at a power density of 750 W kg^{-1}, which holds great promise for practical applications in energy storage.

2. Experimental section

2.1 Synthesis of high quality graphene on nickel foam

In a typical experiment, the graphene was grown on nickel foam (NF, 20 mm × 20 mm × 0.5 mm) by ambient pressure chemical vapor deposition at the temperature of 1050 °C using methane as a carbon source according to a previously reported method.[26] The nickel foam was carefully cleaned with 2 M HCl solution in an ultrasound bath for 30 min in order to remove the NiO layer on the surface, and then rinsed with de-ionized water and absolute ethanol. Before growth, the nickel foam was annealed at 1050 °C for 60 min under a hydrogen flow rate of 100 sccm. Thereafter, the H_2 flow rate was reduced to 40 sccm, and a gas mixture of CH_4 (6 sccm) and Ar (1500 sccm) was purged into the tube furnace. After 10 min of growth, the system was rapidly cooled to room temperature by maintaining the gas rate. Careful weighing revealed that approximately 0.45 mg graphene was obtained on each G/NF sample.

2.2 Electrodeposition of nickel–cobalt hydroxide

The electrodeposition was conducted on a Par 2273 Potentiostat Electrochemistry Workstation (U.S.A.) using a conventional three-electrode system consisting of as-prepared graphene/nickel foam (G/NF) with an effective geometric area of 20 mm × 20 mm as the working electrode, a platinum wire as the counter electrode, and Ag/AgCl as the reference electrode. Bimetallic nickel–cobalt hydroxides were electrodeposited upon G/NF at a constant current with the time of 30 min in aqueous solution containing x mM $Ni(NO_3)_2$ and $(15 - x)$ mM $Co(NO_3)_2$ at ambient temperature. The currents were 1.0, 2.5, 4.0, and 8.0 mA, and the molar ratios of $Ni(NO_3)_2$ and $Co(NO_3)_2$ in the electrodeposition electrolyte were 2 : 1, 1 : 1, and 1 : 2. After electrodeposition, the as-prepared samples were carefully rinsed several times with distilled water and absolute ethanol, with the assistance of ultrasonication to remove any residual electrolyte deposition, and then dried at 60 °C in an oven. Approximately 2.45 mg of NCH was obtained for each sample.

The corresponding NCH/G/NF samples synthesized in a series of electrodeposition electrolytes with different Ni–Co molar ratios were denoted as NCH21/G/NF (2 : 1), NCH11/G/NF (1 : 1), and NCH12/G/NF (1 : 2), respectively.

2.3 Fabrication of an asymmetric supercapacitor

An asymmetric supercapacitor was fabricated based on the NCH11/G/NF electrode as the positive electrode, the activated carbon (AC) electrode as the negative electrode, and polypropylene (PP) fiber as the separator. The negative electrode was prepared as follows: AC, carbon black, and polyvinylidene fluoride (PVDF) binder in a weight ratio of 80 : 10 : 10 were mixed in ethanol and then pasted onto a nickel foam current collector (20 mm × 20 mm). The mass ratio of positive electrode to negative electrode was decided according to the well-known charge balance theory ($q^+ = q^-$).[5] In the relationship, the charge stored by each electrode usually depends on the specific capacitance (C), the potential window (Δv), and the mass of active material (m), as shown in eqn (1):

$$q = C \times \Delta v \times m \quad (1)$$

In order to obtain $q^+ = q^-$, the mass balancing will be expressed as eqn (2):

$$\frac{m^+}{m^-} = \frac{C^- \times \Delta v^-}{C^+ \times \Delta v^+} \quad (2)$$

Based on the specific capacitances of the NCH11/G/NF electrode and AC electrode, the optimal mass ratio between the two electrodes was calculated to be approximately $m^-/m^+ = 3.2$ in the asymmetric supercapacitor.

2.4 Characterization

Powder X-ray diffraction (XRD, Rigaku D/Max 2200 PC, Cu Kα) was conducted to characterize the crystalline structure. Raman spectroscopy was recorded on a DXR Raman microscope with an excitation length of 532 nm. X-ray photoelectron spectroscopy (XPS) analysis was conducted using a twin anode gun, Mg Kα (1253.6 eV) (Microlab 310F Scanning Auger Microprobe, VG Scientific Ltd). The morphologies and structures of the products were analyzed by field-emission scanning electron microscopy (FE-SEM, S4800) with energy dispersive spectrometry (EDS, Oxford, INCAx-act) and transmission electron microscopy (TEM, JEOL JEM-2100F). The elemental composition of Ni and Co in the prepared samples was analyzed employing atomic absorption spectrophotometry (AAS, PerkinElmer 5000).

The electrochemical properties of the materials were characterized using a three-electrode system in 2 M KOH aqueous solution at room temperature. The as-prepared NCH/G/NF was used as the working electrode. Each working electrode had the same area of 20 mm × 20 mm with the weight of the total active materials approximately 2.9 mg (2.45 mg NCH and 0.45 mg graphene). Platinum wire was used as the counter electrode and Hg/HgO as the reference electrode. The electrochemical impedance spectrum (EIS) was tested by applying an AC voltage with 5 mV amplitude in a frequency range from 0.01 Hz to 100 kHz using a 1260-1470E-1455A electrochemical workstation (Solartron, U.S.A). The cyclic voltammetry (CV) at −0.1 to 0.6 V was performed on a CHI660D workstation (CH Instruments, Inc.). The galvanostatic charge and discharge tests were carried out in the potential range of 0–0.5 V on a LAND CT2001 battery tester. The specific capacitances C_s were calculated from the galvanostatic discharge curves using the equation:[27,28]

$$C_s = \frac{it}{m\Delta v} \quad (3)$$

where i, t, Δv, and m are the constant current (A), discharge time (s), potential drop during discharge (V), and mass of active materials (g), respectively. The electrochemical properties of the asymmetric supercapacitor were also investigated in 2 M KOH electrolyte but in a two-electrode cell. All of the electrochemical experiments were carried out on a CHI660D workstation and LAND CT2001 battery tester at room temperature. The energy density (E) and power density (P) of the asymmetric supercapacitor are estimated as follows:[29]

$$E = \frac{1}{2} C_s (\Delta v)^2 \quad (4)$$

$$P = \frac{E}{t} \quad (5)$$

where C_s (F g^{-1}) is the specific capacitance, t (s) is the discharge time (s), and Δv (V) is the potential change during the discharge process.

3. Results and discussion

3.1 Synthesis and structural analysis

The XRD pattern of NCH powders that were scraped from the NCH/G/NF electrodes are illustrated in Fig. S1.† The pattern confirms the existence of Ni–Co binary hydroxides. The typical SEM image of pristine NF, as shown in Fig. 2a, presents a highly

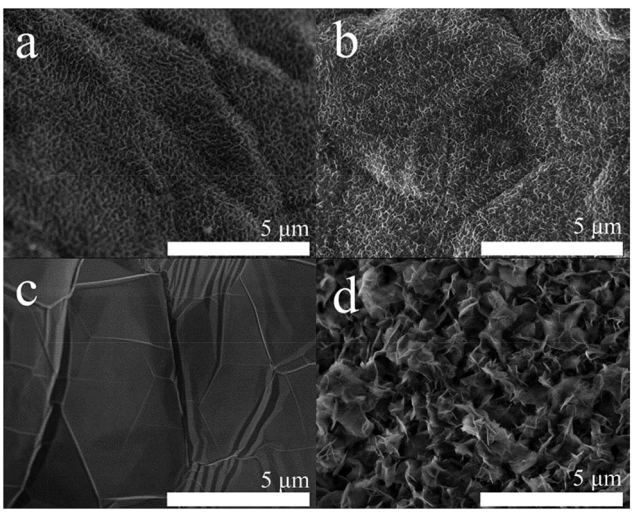

Fig. 2 Typical SEM images of pristine (a) NF, (b) NCH/NF, (c) G/NF, and (d) NCH/G/NF.

textured surface. A large number of nanosized pores can be observed on the surface with some wrinkles. During the ED process, NCH is deposited on the pristine NF, and the morphology of the NCH is similar to the NF (Fig. 2b and S2†). The NCH sheets are tiny and closely packed, which will decrease the liquid–solid interface area and the utilization of active sites. Consequently, the pristine NF is inappropriate to be used as a matrix for the growth of NCH. Fig. 2c shows the morphology of graphene grown on NF *via* the CVD process. Graphene with some wrinkles is coated on the entire surface of NF, which flattens the surface. After the ED process, NCH slices are grown on graphene with a nest-like porous structure (Fig. 2d). The thin slices are uniformly distributed on the graphene with a large surface area. In comparison with NCH on NF, the NCH slices grown on G/NF are bigger and curly, which hinders the aggregation between these slices. The different morphologies of NCH on different matrices demonstrate that the graphene has a positive effect on constructing the 3D porous structure. This hybrid nanostructure ensures (i) improved electronic conductivity due to high quality graphene and NF, (ii) enhanced ionic conductivity due to the porous network, (iii) high utilization of active sites on the enlarged surface area, and (iv) optimized ion transport property by avoiding the binder and conductive agent.

Further examination with XPS illustrates the detailed information regarding elements and oxidation states of the as-prepared NCH/G/NF electrodes (Fig. S3†). In the high-resolution C1s spectra of NCH/G/NF (Fig. S3d†), the absorbance band intensity of C–C is strong with little existence of oxygen-containing functional groups, demonstrating the high quality of the graphene. The broad peak of O 1s is centered at 532 eV, which is associated with bound hydroxide groups (OH^-) and confirms the formation of Ni–Co binary hydroxides (Fig. S3e†).[30] The Ni 2p and Co 2p spectra both show two spin–orbit doublets with shakeup satellites peaks (Fig. S3f and S3g†), illustrating that NCH is composed of Ni^{2+}, Ni^{3+}, Co^{2+}, and Co^{3+}.

In order to further demonstrate the quality of the graphene and its stability, Raman spectra were obtained for different samples. The G band (approximately 1590 cm^{-1}) is attributed to the vibration of sp^2-bonded carbon atoms, while the D band (approximately 1350 cm^{-1}) arises from disorders or defects, and the 2D band at approximately 2700 cm^{-1} originates from a double-resonance process.[31–34] As exhibited in Fig. 3, only G and 2D bands can be observed in the G/NF and NCH/G/NF electrodes, which confirms the high structural quality of the defect-free graphene.[35] Moreover, the integrated intensity ratio between the G and 2D bands (I_G/I_{2D}) reveals that the graphene has few layers.[36] During the ED process, the I_G/I_{2D} ratio retains a similar value. The results also demonstrate that high-quality graphene is maintained during the ED process. Because the pure NF has no peaks, the peaks at approximately 500 cm^{-1} are confirmed to be NCH. High quality graphene will significantly improve the conductivity,[37] and thus, high cycling stability is expected.

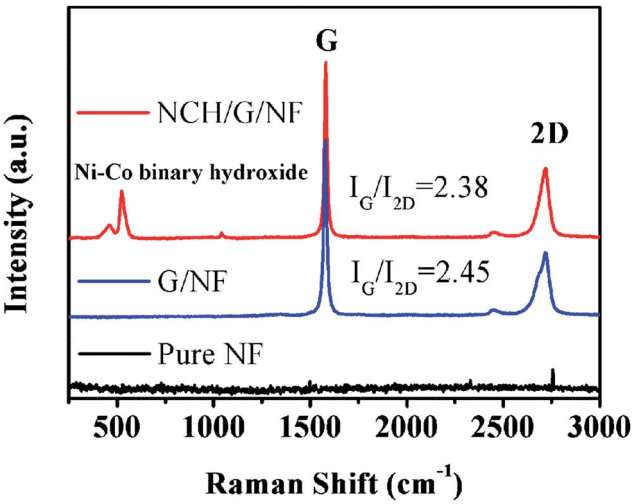

Fig. 3 Raman spectroscopy of pristine NF, G/NF, and NCH/G/NF.

3.2 The effect of deposition current density

The morphology and microstructure of electrode materials, decided by the ED process, have a great effect on the electrochemical performance. Among all the synthesis conditions, the deposition current density has a large influence on the growth process of NCH slices, which is discussed firstly. Fig. 4 shows the morphologies of NCH/G/NF electrodes prepared at different current densities. At a low current density of 0.25 mA cm^{-2}, NCH particles with the size of 100–200 nm are formed (Fig. 4a). These particles contact each other tightly, showing the trend to form sheets. The compact structure with a small number of pores will decrease the active sites for redox reaction. When the current density increases to 0.625 mA cm^{-2}, NCH grows into thin sheets with a large size (Fig. 4b). Numerous pores are created between the neighboring nanosheets for ion transport. The loose and porous structure enlarges the surface area to increase the active sites, and the thin sheets will also shorten the electron transportation distance. Fig. 4c displays the NCH sheets prepared at 1 mA cm^{-2}, which are thicker and tightly assemble

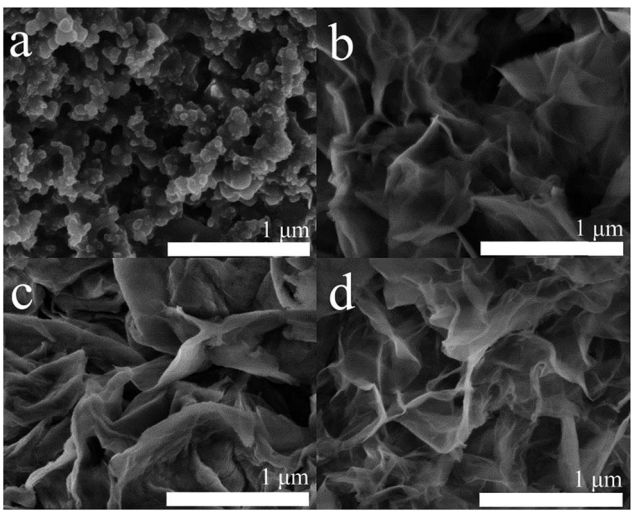

Fig. 4 SEM images of NCH/G/NF prepared at different ED current densities, (a) 0.25 mA cm^{-2}, (b) 0.625 mA cm^{-2}, (c) 1 mA cm^{-2}, and (d) 2 mA cm^{-2}.

together. At 2 mA cm^{-2}, the structure of NCH becomes more compact (Fig. 4d). These two compact textures will decrease the contact area with the electrolyte and active sites for redox reaction. The probable reason for the formation of different morphologies is as follows. At low current density, the total quantity of electric charge is small, which restricts the growth of NCH due to the relatively low rate of reaction. When the current density increases, the electrode can obtain more electrons and ions to form NCH sheets. However, at high current density, more Ni and Co ions transform to NCH, and the structure become compact.

3.3 The effect of Ni–Co ratio in the deposition solution

The molar ratio of the Ni and Co component not only affects the morphology, but also plays an important role in the capacitance. To exploit the appropriate conditions, NCH/G/NF electrodes in different Ni–Co ratio solutions were prepared. Fig. 5 shows the SEM images of NCH21/G/NF (a and b), NCH11/G/NF (c and d), and NCH12/G/NF (e and f) electrodes. All electrodes exhibited a 3D network-like structure composed of numerous nanosheets interconnected with each other. Furthermore, abundant open spaces between the adjacent nanosheets can be observed. However, as the Co content increases, the open spaces become larger and larger due to the increasing size of the nanosheets. Typical hexagonal sheet-like structures are formed from the stable $Co(OH)_2$.[38,39] However, there are some nanoscale-sized mesopores on the NCH12 sheets (Fig. 5e and f) that result from the release of gaseous species during the decomposition process.[40] The NCH12 sheets are easily damaged from bulk effects during the redox process by these mesopores. The compact structure and small open spaces of NCH21/G/NF (Fig. 5a and b) will also decrease the active sites for redox reaction. However, the integrated nanosheets and large open spaces of NCH11/G/NF will enlarge the surface area and shorten the diffusion path of ions and electrons to enhance the redox kinetics. TEM images of these samples also confirm that the size of the nanosheets becomes larger and larger when the Ni–Co ratio increases (Fig. S4†). The selected area electron diffraction (SAED) results of all the samples show well-defined and sharp diffraction rings, meaning that the NCHs are polycrystalline. From EDS mapping images (inset in Fig. 2b, d and f), the distribution of Ni and Co components are confirmed to be uniform over all the NCH/G/NF electrodes. The Ni–Co ratios in the prepared NCHs were also analyzed by AAS, and the results are displayed in Table 1. The Ni–Co ratios in the NCHs are less than their counterparts in the deposition electrolyte, which is consistent with a previously reported result[38] and probably has occurred because of the different solubility product constants of $Ni(OH)_2$ and $Co(OH)_2$.

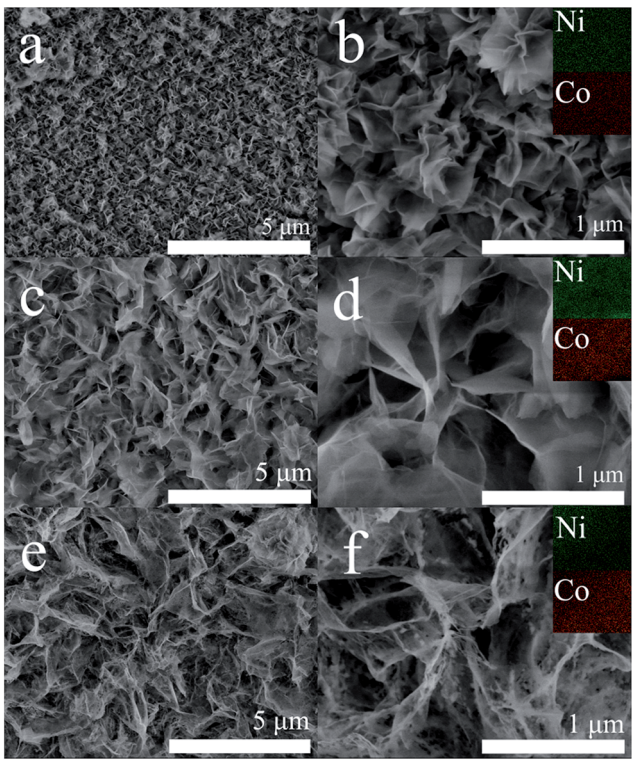

Fig. 5 SEM images of NCH/G/NF prepared in different Ni–Co ratio solutions, (a and b) NCH21/G/NF, (c and d) NCH11/G/NF, and (e and f) NCH12/G/NF. The insets in (b, d, and f) show the element (Ni and Co) mapping of these samples.

3.4 Electrochemical characterization

In order to further certify the superiority of the 3D porous NCH/G/NF electrodes, the electrochemical performance of different electrodes was measured. Fig. 6a shows the CV curves of the G/NF substrate, NCH/NF electrode, and NCH/G/NF electrode. Each NCH/NF and NCH/G/NF electrode shows a pair of obvious large redox peaks, corresponding to the reversible redox reaction related to M–O/M–O–OH, where M represents Ni and Co ions.[24,41] According to the equation for specific capacitance ($C = \int I dV/2\Delta vs$), a larger area surrounded by the CV curve relates to a higher specific capacitance. The CV curve of the NCH/G/NF electrode shows a larger area than that of the curve for the NCH/NF electrode. In addition, the anodic and cathodic peaks of NCH/G/NF show a greater symmetrical shape, and the peak separation is smaller. These phenomena suggest that enhanced capacitance and higher redox reversibility of the NCH/G/NF electrode are obtained by the addition of high quality graphene. The G/NF substrate exhibits very low charge capability, illustrating that the double-layer capacitance of graphene is contributing little to the total capacitance. Fig. 6b displays the CV curves of NCH/G/NF electrodes prepared at different deposition current densities. The CV curve of the NCH/G/NF electrode prepared at 0.625 mA cm^{-2} clearly shows the largest

Table 1 The molar ratio of Ni and Co in the electrodeposition electrolyte and the prepared NCH/G/NF (according to AAS results)

Samples	Molar ratio in the electrodeposition electrolyte (Ni–Co)	Molar ratio in NCH (Ni–Co)
NCH21/G/NF	2 : 1	1.83 : 1
NCH11/G/NF	1 : 1	0.87 : 1
NCH12/G/NF	1 : 2	0.92 : 2

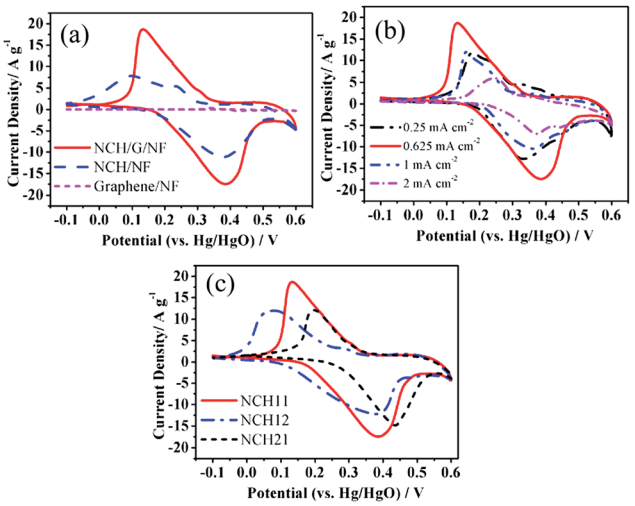

Fig. 6 (a) CV curves of G/NF, NCH/NF, and NCH/G/NF electrodes at a scan rate of 5 mV s^{-1}. (b) CV curves of NCH/G/NF electrodes prepared at different deposition current densities at a scan rate of 5 mV s^{-1}. (c) CV curves of electrodes with different Ni–Co ratios at a scan rate of 5 mV s^{-1}.

surrounding area, indicating the highest specific capacitance. The enhanced capacitance benefits from increased active sites due to the 3D porous structure of the large nanosheets and open spaces. The most suitable current density is 0.625 mA cm^{-2}, which is consistent with the SEM analysis. The effect of the Ni–Co ratio in the deposition solution is also discussed. As shown in Fig. 6c, all the CV curves of the samples at different ratios show typical pseudo-capacitive shapes with symmetric redox peaks, indicating that there is good redox reversibility. The curve of the NCH21/G/NF electrode shows a smaller area due to the compact structure, which has less active sites. It has been reported that the addition of Co will reduce the specific capacitance,[38] and therefore, the NCH12/G/NF electrode with a high Co content also shows a relatively low capacitance. Taking into effect the dual effects of porous structure and Ni–Co ratio, the NCH11/G/NF electrode shows an enhanced capacitance compared with the other two electrodes.

A series of charge and discharge measurements was conducted on different electrodes at various currents. Fig. 7a exhibits the discharge curves of NCH/G/NF electrodes prepared at different deposition current densities. Based on eqn (3) for calculating specific capacitance, a longer discharge time denotes a higher capacitance. The NCH/G/NF electrode prepared at 0.625 mA cm^{-2} shows the longest discharge time, which is in accordance with the CV results. For electrodes with different Ni–Co ratios (Fig. 7b), all the electrodes displayed typical pseudo-capacitive behavior with highly nonlinear discharge curves. All the curves show the obvious discharge voltage plateaus, which match well with the reduction peaks observed in the CV curves (Fig. 6c). Fig. 7c shows discharge curves of electrodes with different Ni–Co ratios at various current densities of 2, 4, 8, and 20 A g^{-1}. The NCH11/G/NF electrode exhibits the highest capacitance performance. Calculations determined the specific capacitances of the

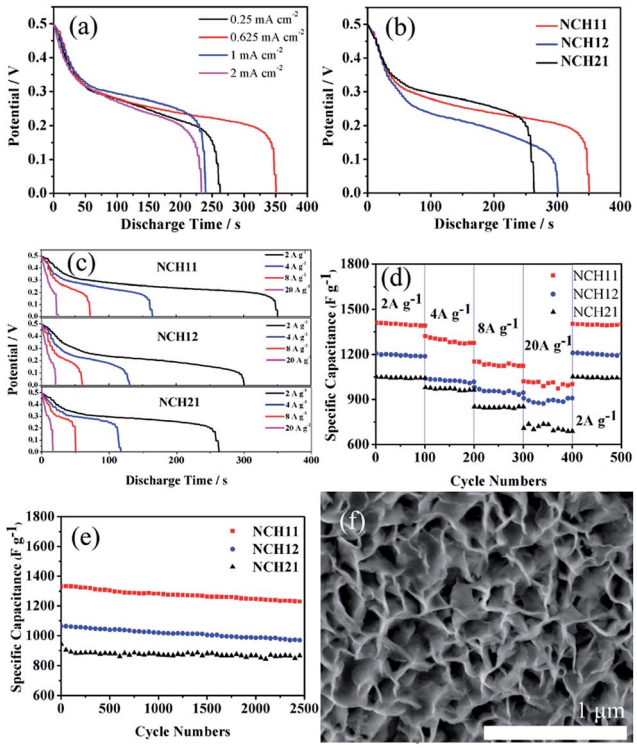

Fig. 7 (a) Galvanostatic discharge curves at 2 A g^{-1} of NCH/G/NF electrodes prepared at different deposition current densities. (b) Galvanostatic discharge curves at 2 A g^{-1} of electrodes with different Ni–Co ratios. (c) Galvanostatic discharge curves of electrodes with different Ni–Co ratios at various discharge current densities. (d) Rate capacitance of electrodes with different Ni–Co ratios with increasing current densities. (e) Cyclic performance of electrodes with different Ni–Co ratios at 4 A g^{-1}. (f) SEM image of the NCH11 electrode after a charging and discharging test of 2500 cycles.

NCH21/G/NF, NCH11/G/NF, and NCH12/G/NF electrodes, which are 1050, 1410, and 1210 F g^{-1} at 2 A g^{-1}, respectively. Even at the high current density of 20 A g^{-1}, the specific capacitance of the NCH11/G/NF electrode is still over 1000 F g^{-1}. To further analyze the rate capacity, the capacitances at various current densities are shown in Fig. 7d. At 4 A g^{-1}, the capacitances are 984, 1328, and 1056 F g^{-1} for the NCH21/G/NF, NCH11/G/NF, and NCH12/G/NF electrodes with high rate retentions of 93.5%, 94.6%, and 87.7%, respectively. At 20 A g^{-1}, the capacitance loss of the NCH11/G/NF electrode is as low as 25.9%, which is still lower than those of 31.6% and 27.1% for the NCH21/G/NF and NCH12/G/NF electrodes, respectively. The compact structure and low Co ratio of NCH21 and the mesopores on the NCH12 sheets lead to the relatively poor rate capacity. Fig. 7e exhibits the cyclability of the electrodes at 4 A g^{-1}. After 2500 cycles, the capacitance retention ratios of the NCH21/G/NF, NCH11/G/NF, and NCH12/G/NF electrodes are 91.7%, 92.1%, and 91.2%, respectively. The high rate capacity and stability of these 3D porous electrodes are at a higher level than those previously reported in the literature (Table S1 and S2†) and much higher than those of traditional electrodes composed of powders.[42,43] Fig. 7f displays the SEM image of the NCH11/G/NF electrode after 2500 cycles of testing. During the

cyclic test, the porous structure is well maintained, which is the primary reason for the perfect stability.

Electrochemical impedance spectroscopy (EIS) is an effective method to evaluate the electron transport properties of an electrochemical system. Fig. 8 shows the Nyquist plots of the NCH21, NCH11, and NCH12 electrodes. The inset shows the semicircle evident at high frequencies. All of the spectra display depressed semicircles in the high-frequency region and straight lines in the low-frequency region. In the high-frequency region, the semicircle corresponds to the charge transfer resistance at the electrode/electrolyte interface, which is related to the surface area and electrical conductivity.[44,45] Among the three electrodes, NCH11 displays the smallest radius, which illustrates its lowest charge transfer resistance. The low resistance is ascribed to the integrated nanosheets and large open spaces of NCH11. In the low frequency region, the straight line reflects the diffusion of the electroactive species.[46] The nearly vertical line indicates rapid ion diffusion in the electrolyte and adsorption onto the electrode surface.[23] All of the electrodes show a large slope, demonstrating that the structure of these 3D porous networks is suitable for rapid ion diffusion. These results are in good accordance with the above-mentioned high rate capability.

Based on the above analyses, 3D porous NCH/G/NF binder-free electrodes showed excellent capacitive and cycling performance even at considerably high charge and discharge currents. The reason for the excellent performance can be well understood if the following factors are considered. Firstly, high quality graphene provides an effective conductive network for fast ion and electron transport. Secondly, the 3D porous structure is beneficial for enlarging the contact area with electrolyte and increasing the number of active sites for redox reactions. Thirdly, the optimum Ni–Co ratio leads to large open spaces and less micropores on the sheets, which increase the active sites and improve the stability. Fourthly, binder-free electrodes improve the conductivity by avoiding the usage of binder.

3.5 Electrochemical properties of the asymmetric supercapacitor

To further illustrate the potential application of the binder-free NCH/G/NF electrodes, an asymmetric supercapacitor was fabricated. Fig. 9a exhibits the typical CV curves of the asymmetric supercapacitor at different scan rates. The CV curves show a collective contribution of electric double-layer capacitance and pseudocapacitance at 0–1.5 V. When the scan rate increases from 5 to 100 mV s^{-1}, the CV curves retain a similar shape, indicating high fast charge–discharge properties of the device.[47] Fig. 9b shows the charge and discharge curves of the asymmetric supercapacitor. At different current densities, symmetric triangular-shaped curves are clearly observed, suggesting a rapid *I*–*V* response. The specific capacitance based on the total mass was calculated according to eqn (3). At 1, 2, 4, and 10 A g^{-1}, the specific capacitances are 108, 94.7, 80, and 66.7 F g^{-1}, respectively. The capacitance retention is 61.7% when the current density increases from 1 to 10 A g^{-1}. As shown in the Ragone plot (Fig. 9c), a high energy density of 33.75 W h kg^{-1} at the power density of 750 W kg^{-1} and a high power density of 7500 W kg^{-1} was obtained at the energy density of 20.84 W h kg^{-1}. The maximum energy density of our asymmetric supercapacitor is higher than those of previously reported devices (<25 W h kg^{-1}).[47–49] The durability of the as-fabricated asymmetric supercapacitor was also evaluated. As displayed in Fig. 9d, the capacitance retention rate is 84.4% of its original capacitance after 2000 cycles, which is comparable to those of other asymmetric supercapacitors.[29] The above performance indicates that the binder-free NCH/G/NF electrode is promising as an attractive candidate for energy storage.

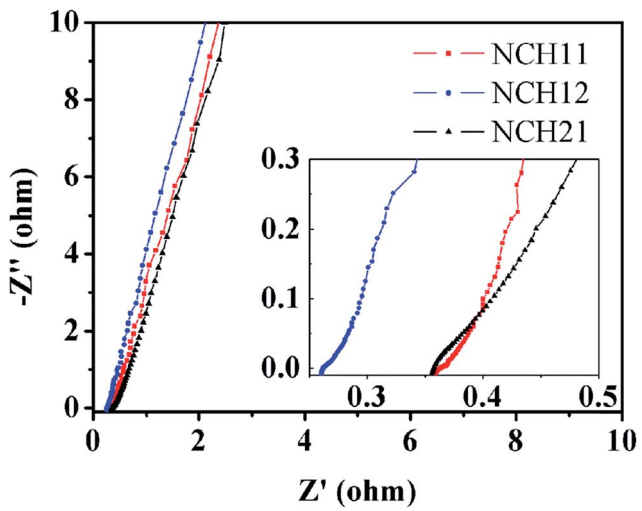

Fig. 8 Electrochemical impedance spectra (EIS) obtained from the NCH21/G/NF, NCH11/G/NF, and NCH12/G/NF electrodes. The inset shows the enlarged EIS of the electrodes.

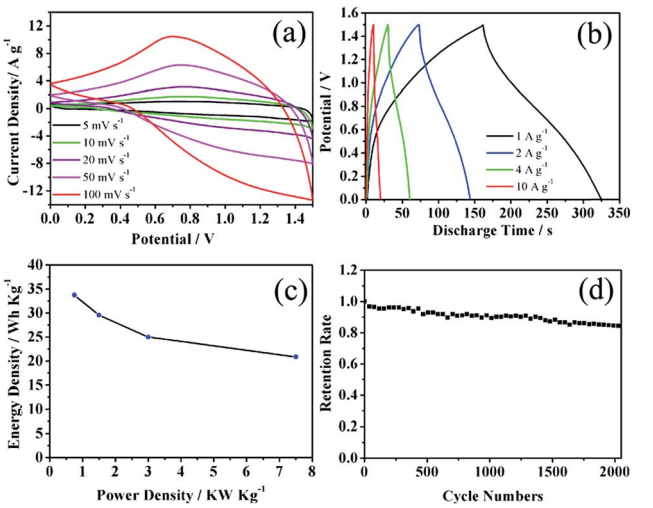

Fig. 9 Electrochemical performance of the asymmetric supercapacitor measured in 2 M KOH electrolyte. (a) CV curves at different scan rates, (b) discharge profiles at different current densities, (c) Ragone plot related to energy and power densities, and (d) cycling stability at 4 A g^{-1}.

4. Conclusions

We have successfully fabricated binder-free NCH/G/NF electrodes for supercapacitors *via* a CVD and ED process. The binder-free electrodes can increase the mass of efficient active material and the conductivity. Graphene was covered on the rough surface of NF to make the surface flat, which is beneficial to the formation of the 3D porous architecture. The 3D structure enhances the electron transport ability and enables more active sites to sufficiently make contact with electrolyte. Furthermore, the morphology of NCH can be controlled by adjusting the deposition current density and the Ni–Co ratio of the deposition solution. As a result, at optimized conditions, the NCH11/G/NF electrode shows the highest capacitance and the optimal stability. Additionally, the as-fabricated asymmetric supercapacitor delivers a prominent energy density of 33.75 W h kg^{-1}. The excellent performance results from the synergetic effect of the unique 3D porous structure and enhanced conductivity. These results illustrate that binder-free NCH/G/NF electrodes are promising for use in supercapacitors.

Acknowledgements

This work is supported by the National Basic Research Program of China (2012CB932303) and the National Natural Science Foundation of China (Grants no. 51072215 and 51172261).

Notes and references

1 L. Yu, G. Q. Zhang, C. Z. Yuan and X. W. Lou, *Chem. Commun.*, 2013, **49**, 137–139.
2 H. Chen, L. F. Hu, M. Chen, Y. Yan and L. M. Wu, *Adv. Funct. Mater.*, 2014, **24**, 934–942.
3 G. Wang, L. Zhang and J. Zhang, *Chem. Soc. Rev.*, 2012, **41**, 797–828.
4 Y. Zhai, Y. Dou, D. Zhao, P. F. Fulvio, R. T. Mayes and S. Dai, *Adv. Mater.*, 2011, **23**, 4828–4850.
5 J. Yan, Z. J. Fan, W. Sun, G. Q. Ning, T. Wei, Q. Zhang, R. F. Zhang, L. J. Zhi and F. Wei, *Adv. Funct. Mater.*, 2012, **22**, 2632–2641.
6 C. Zhao, X. Wang, S. Wang, Y. Wang, Y. Zhao and W. Zheng, *Int. J. Hydrogen Energy*, 2012, **37**, 11846–11852.
7 Z. Lu, Q. Yang, W. Zhu, Z. Chang, J. Liu, X. Sun, D. G. Evans and X. Duan, *Nano Res.*, 2012, **5**, 369–378.
8 Y. Wang, H. Liu, X. Sun and I. Zhitomirsky, *Scr. Mater.*, 2009, **61**, 1079–1082.
9 R. B. Rakhi, W. Chen and H. N. Alshareef, *J. Mater. Chem.*, 2012, **22**, 5177–5183.
10 L. L. Zhang and X. S. Zhao, *Chem. Soc. Rev.*, 2009, **38**, 2520–2531.
11 Z. S. Wu, W. Ren, D. W. Wang, F. Li, B. Liu and H. M. Cheng, *ACS Nano*, 2010, **4**, 5835–5842.
12 M. Noked, A. Soffer and D. Aurbach, *J. Solid State Electrochem.*, 2011, **15**, 1563–1578.
13 G. Hu, C. Tang, C. Li, H. Li, Y. Wang and H. Gong, *J. Electrochem. Soc.*, 2011, **158**, A695–A699.
14 H. Gao, G. Wang, M. Yang, X. Zhang, Z. Shi, C. Li, X. Zhang and X. Cui, *RSC Adv.*, 2013, **3**, 2604–2612.
15 J. H. Zhong, A. L. Wang, G. R. Li, J. W. Wang, Y. N. Ou and Y. X. Tong, *J. Mater. Chem.*, 2012, **22**, 5656–5665.
16 J. Chen, D. H. Bradhurst, S. X. Dou and H. K. Liu, *J. Electrochem. Soc.*, 1999, **146**, 3606–3612.
17 X. Y. Liu, Y. Q. Zhang, X. H. Xia, S. J. Shi, Y. Lu, X. L. Wang, C. D. Gu and J. P. Tu, *J. Power Sources*, 2013, **239**, 157–163.
18 H. Yang, G. H. Guai, C. Guo, Q. Song, S. P. Jiang, Y. Wang, W. Zhang and C. M. Li, *J. Mater. Chem. C*, 2011, **115**, 12209–12215.
19 X. H. Xia, J. P. Tu, Y. J. Mai, R. Chen, X. L. Wang, C. D. Gu and X. B. Zhao, *Chem.–Eur. J.*, 2011, **17**, 10898–10905.
20 P. Lin, Q. J. She, B. L. Hong, X. A. J. Liu, Y. N. Shi, Z. Shi, M. S. Zheng and Q. F. Dong, *J. Electrochem. Soc.*, 2010, **157**, A818–A823.
21 H. L. Wang, H. S. Casalongue, Y. Y. Liang and H. J. Dai, *J. Am. Chem. Soc.*, 2010, **132**, 7472–7477.
22 X. Zhu, H. Dai, J. Hu, L. Ding and L. Jiang, *J. Power Sources*, 2012, **203**, 243–249.
23 M. Kim, Y. Hwang and J. Kim, *J. Power Sources*, 2013, **239**, 225–233.
24 C. Yuan, J. Li, L. Hou, X. Zhang, L. Shen and X. W. D. Lou, *Adv. Funct. Mater.*, 2012, **22**, 4592–4597.
25 Y. Li, P. Hasin and Y. Wu, *Adv. Mater.*, 2010, **22**, 1926–1929.
26 H. Zheng, T. Zhai, M. Yu, S. Xie, C. Liang, W. Zhao, S. Wang, Z. Zhang and X. Lu, *J. Mater. Chem. C*, 2013, **1**, 225–229.
27 J. Z. Sheng Chen, X. Wu, Q. Han and X. Wang, *ACS Nano*, 2010, **4**, 2822–2830.
28 H. Xia, Y. S. Meng, G. Yuan, C. Cui and L. Lu, *Electrochem. Solid-State Lett.*, 2012, **15**, A60–A63.
29 H. Chen, L. Hu, M. Chen, Y. Yan and L. Wu, *Adv. Funct. Mater.*, 2014, **24**, 934–942.
30 U. M. Patil, J. S. Sohn, S. B. Kulkarni, S. C. Lee, H. G. Park, K. V. Gurav, J. H. Kim and S. C. Jun, *ACS Appl. Mater. Interfaces*, 2014, **6**, 2450–2458.
31 F. Yang, Y. Liu, L. Gao and J. Sun, *J. Phys. Chem. C*, 2010, **114**, 22085–22091.
32 C.-Y. Su, Y. Xu, W. Zhang, J. Zhao, X. Tang, C.-H. Tsai and L.-J. Li, *Chem. Mater.*, 2009, **21**, 5674–5680.
33 M. Li, J. E. Zhu, L. Zhang, X. Chen, H. Zhang, F. Zhang, S. Xu and D. G. Evansa, *Nanoscale*, 2011, **3**, 4240–4246.
34 H. Li, G. Zhu, Z.-H. Liu, Z. Yang and Z. Wang, *Carbon*, 2010, **48**, 4391–4396.
35 H. Bukowska, F. Meinerzhagen, S. Akcöltekin, O. Ochedowski, M. Neubert, V. Buck and M. Schleberger, *New J. Phys.*, 2011, **13**, 063018.
36 W. Liu, C. Lu, X. Wang, K. Liang and B. K. Tay, *J. Mater. Chem. A*, 2015, **3**, 624–633.
37 I. W. P. Chen, S.-H. Saint Jhou and Y.-W. Chen, *J. Mater. Chem. C*, 2013, **1**, 5970–5975.
38 Y.-M. Wang, X. Zhang, C.-Y. Guo, Y.-Q. Zhao, C.-L. Xu and H.-L. Li, *J. Mater. Chem. A*, 2013, **1**, 13290.
39 C. Yuan, L. Yang, L. Hou, L. Shen, X. Zhang and X. W. Lou, *Energy Environ. Sci.*, 2012, **5**, 7883–7887.
40 H. B. Wu, H. Pang and X. W. Lou, *Energy Environ. Sci.*, 2013, **6**, 3619–3626.
41 V. Gupta, S. Gupta and N. Miura, *J. Power Sources*, 2008, **175**, 680–685.

42 S.-K. Chang, Z. Zainal, K.-B. Tan, N. A. Yusof, W. M. D. W. Yusoff and S. R. S. Prabaharan, *Curr. Appl. Phys.*, 2012, **12**, 1421–1428.
43 W. H. Wen, H. Z. Ai, C. Y. Qin, C. Y. Li, W. H. Ying, Z. Z. Yu and Y. Y. Ying, *J. Mater. Chem.*, 2011, **21**, 10504–10511.
44 S.-E. Chun, S.-I. Pyun and G.-J. Lee, *Electrochim. Acta*, 2006, **51**, 6479–6486.
45 Y.-Y. Horng, Y.-C. Lu, Y.-K. Hsu, C.-C. Chen, L.-C. Chen and K.-H. Chen, *J. Power Sources*, 2010, **195**, 4418–4422.
46 L. Wang, Z. H. Dong, Z. G. Wang, F. X. Zhang and J. Jin, *Adv. Funct. Mater.*, 2013, **23**, 2758–2764.
47 X. Wang, A. Sumboja, M. Lin, J. Yan and P. S. Lee, *Nanoscale*, 2012, **4**, 7266–7272.
48 H. Wang, C. M. B. Holt, Z. Li, X. Tan, B. S. Amirkhiz, Z. Xu, B. C. Olsen, T. Stephenson and D. Mitlin, *Nano Res.*, 2012, **5**, 605–617.
49 C. Tang, Z. Tang and H. Gong, *J. Electrochem. Soc.*, 2012, **159**, A651–A656.

